A.5 Energy estimation by the least squares method

Now, that we established our separation methods, we would like to use the selected events to calculate the physical quantities that we are interested in. The first step is to estimate the energy from the image parameters and to determine the energy resolution that we can get for CT1.

Here I use a very simple method based on image parameters and the ***method of linear least squares*** to ***estimate the energy***. As we will see, the formalism is quite similar to that of the LDA.

The method of linear least squares and its application

We have a set of parameters for each event i

$$\overrightarrow{p^i} = \begin{pmatrix} 1 \\ p_1^i \\ \vdots \\ p_n^i \end{pmatrix} \equiv \mathbf{P}_k^i \tag{A.81}$$

which parameterize the image. The 'ONE' in the first row is important as it is needed for the offset. We wish to find an estimator E_{est}^i for the energy E^i of each event i in such a way that the ***sum of differences***

$$S = \sum (E_{est}^i - E^i)^2 \tag{A.82}$$

with the linear ansatz

$$E_{est}^i = \mathbf{P}_k^i w^k \tag{A.83}$$

being ***minimal.*** This is the case if

$$\frac{\partial S}{\partial p_j} = 2\left(\mathbf{P}^T\right)_i^j \left(\mathbf{P}_k^i w^k - E^i\right) = 0 \tag{A.84}$$

$$\left[\left(\mathbf{P}^T\right)_i^j \mathbf{P}_k^i\right] w^k = \left(\mathbf{P}^T\right)_i^j E^i \tag{A.85}$$

$$w^k = \left[\left(\mathbf{P}^T\right)_i^j \mathbf{P}_k^i\right]^{-1} \left(\mathbf{P}^T\right)_i^j E^i \tag{A.86}$$

This procedure is called ***linear least squares*** and can be ***solved analytically***. (It is almost identical to the calculation of the weights of the LDA. In case of the LDA the E^i correspond to the different groups. For the case of 2 groups it becomes $E^i = -1$ for gammas and $E^i = +1$ for protons. The 'ONE' above corresponds to the subtraction of the average output given by Equ. A.61). It only remains to calculate the ***weights*** w^k using Equ. A.86 which involves the calculation of an ***inverse matrix***. The inverse matrix calculation was done by the Gaussian elimination algorithm using a precision of 24 digits.

The following parameters have been used to estimate the (log) energy.

$$\begin{aligned} p_0 &= \log(SIZE) \\ p_1 &= \sqrt{\log(SIZE)} \\ p_2 &= \log^2(SIZE) \\ p_3 &= \frac{1}{\cos(ZenithAngle)} \\ p_4 &= \log(LENGTH) \\ p_5 &= DIST \end{aligned} \tag{A.87}$$

The ***main estimator is SIZE*** (and expressions of it) which is corrected with the ***cosine of the zenith angle*** (shower distance changes with cosine). The other parameters are introduced to obtain ***small corrections***. SIZE is dependent on the impact parameter (-> estimator DIST). For the training a MC-gamma data sample was used. A preselection cut of $ZenithAngle \leq 50\,deg$, $SIZE \geq 60\,PhE$ and $0.5\,deg \leq DIST \leq 1.05\,deg$ was applied beforehand.

Additional energy dependent ***weights*** $E^{1.5}$ on each event have been introduced in the method to ***correct*** for the fact that the MC was produced with a steep spectrum of $E^{-1.5}$ while we want that high energy events are treated with the ***same priority*** as low energy events. The whole procedure is calculated in the log-scale. Equ. A.85 and Equ. A.86 become:

$$\left[\left(\mathbf{P}^T\right)_i^j \mathbf{P}_k^i \left(E^i\right)^{1.5}\right] w^k = \left(\mathbf{P}^T\right)_i^j \left(E^i\right)^{1.5} \log\left(E^i\right) \quad \text{(A.88)}$$

$$w^k = \left[\left(\mathbf{P}^T\right)_i^j \mathbf{P}_k^i \left(E^i\right)^{1.5}\right]^{-1} \times \left(\mathbf{P}^T\right)_i^j \left(E^i\right)^{1.5} \log\left(E^i\right) \quad \text{(A.89)}$$

The result can be seen in Fig. A.33. SIZE was introduced in parallel with several exponents (1, 0.5 and 2). This improves the ***linearity*** of the estimation.

Improvement of the energy resolution by including the LEAKAGE parameter into the Least square fit

Now we will see how the resolution and the shape can still be improved by introducing a ***new parameter called LEAKAGE*** into the least square fit. It is introduced as an ***additional input*** to the least squares method of Equ. A.87:

$$P_6 = LEAKAGE \quad \text{(A.90)}$$

$$p_7 = LEAKAGE^2 \quad \text{(A.91)}$$

The result can be seen in Fig. A.34. The distribution becomes more ***narrow and Gaussian***. The distribution is not perfectly linear and exhibits a slight curve. Without unfolding the spectrum this would introduce a systematic error. The unfolding procedure corrects for this and in fact any shape of the energy estimation would be translated correctly as long as it is ***monotonically.***

A.5.1 Conclusion about the energy estimation using the linear least squares method

Using an algorithm like ***linear least squares*** to estimate the energy has the main advantage, as the ***LDA***, that the problem is ***analytically solvable*** (reproducibility, no dependence on initial values) unlike other methods like neural nets or nonlinear equations which need an ***iterative*** optimization. A matrix of the size ***8x8*** has to be inverted (best done with 24 digits precision or more). The applied energy estimation is done by calculation of a simple polynomial which is fast. The energy estimation is linear (above 1 TeV) and Gaussian distributed. The introduction of the LEAKAGE parameter ***increases*** the resolution a little and results in an output which is more Gaussian.

A.6 Mispointing of the telescope and its correction

Unfortunately the hour angle axis of the CT1 telescope is ***not perfectly aligned*** with the earths axis of rotation and in addition, the telescope structure bends slightly under its

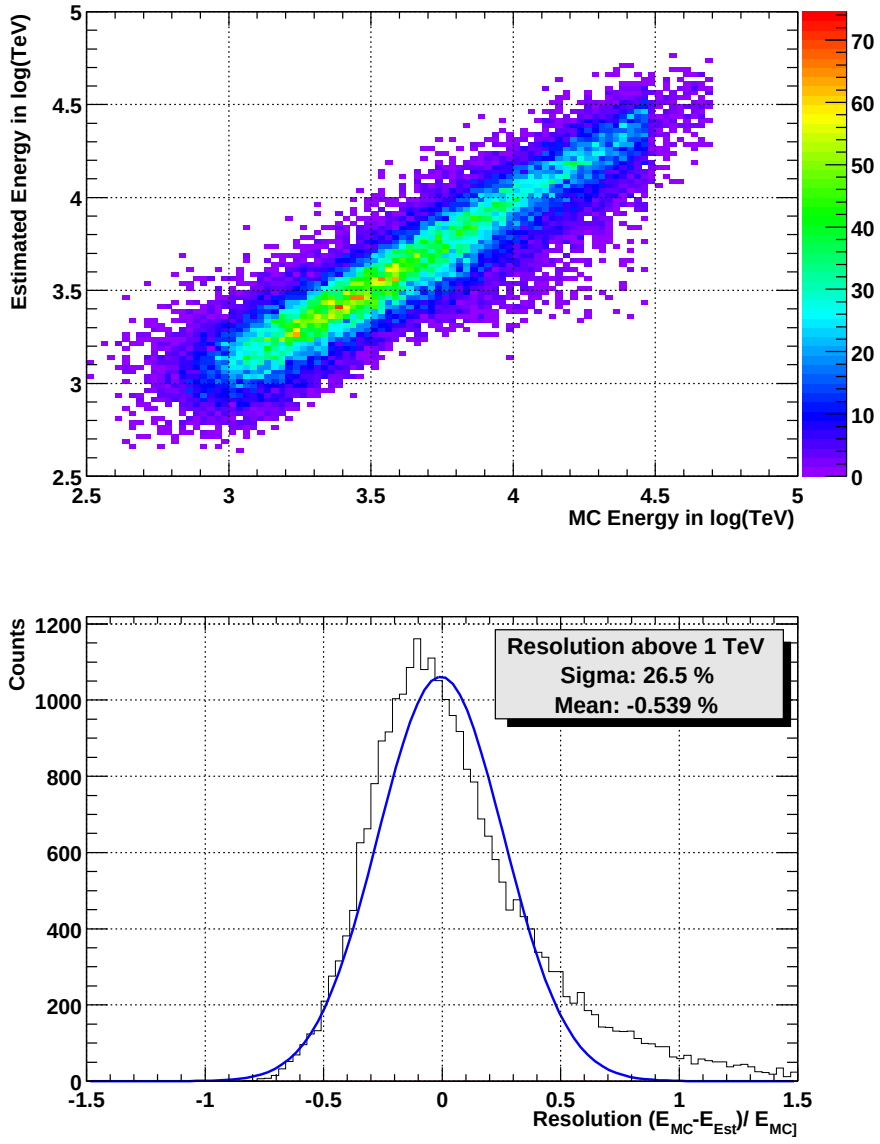

Figure A.33: Energy estimation and its ***resolution*** with the LEAKAGE parameter. For energies above 10 TeV (the upper plot) it can been seen that the effect of truncated images at the camera border disturbs the energy estimation. The lower plots shows a rather asymmetric shape which is not Gaussian.

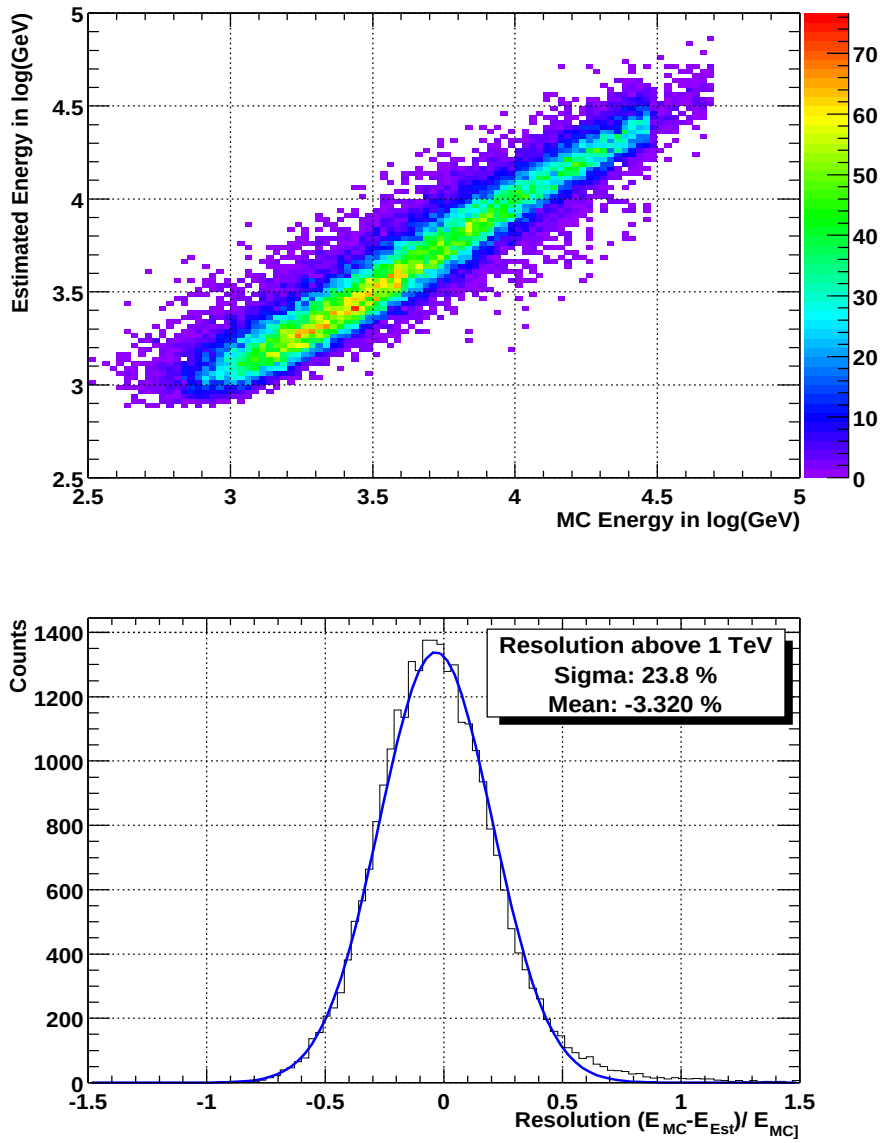

Figure A.34: The shape of the estimated energy distribution ***after*** introduction of the ***LEAKAGE*** parameter. The energy estimation becomes sharper and more precise as can be observed in the upper plot. Above 1 TeV the estimation is very linear. The lower plot demonstrates a symmetric Gaussian distribution with a variance of approximately 24 %.

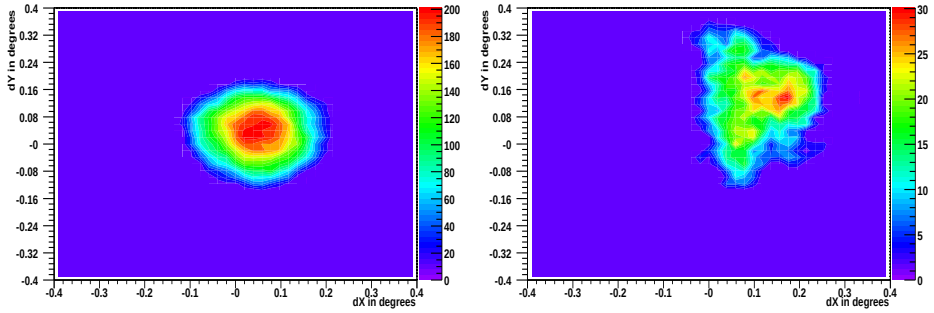

Figure A.35: A false source plot for a) a small zenith angle (15°), used to determine the mispointing of the source Mkn 421. The center of the source appears as a round spot. b) False source plot for a high zenith angle (45°). The source seems not to be focused very well in one point. This effect could be partly due to statistics but a mispointing correction on ***run basis*** results in a ***sharper*** ALPHA distribution, suggesting that for different runs with the ***same*** hour angle (= 'signed' zenith angle) the mispointing is different.

weight. This introduces in a ***mispointing*** of up to ***0.15***° and has a strong effect on the ***sharpness*** of the ALPHA distribution. Monte Carlo studies show that the standard deviation of the ALPHA peak should be approximately 6° for small zenith angles and up to 7.5° for high zenith angles of 45° (showers with higher zenith angles show a wider alpha distribution due to a smaller image in the camera resulting in a worse determination of the shower axis). With Mispointing, these values ***increase*** to a standard deviation of up to ***15***° for high zenith angles. If in such a scenario a fixed alpha cut of only 12° is applied, it is easy to imagine that the measured flux will suddenly depend strongly on the zenith angle. This introduces a ***large systematic error*** in lightcurve calculation. Thus, a pointing correction is mandatory.

Up to now, so-called point-runs have been performed where the telescope systematically scans a star (whose coordinates are known) in small steps. The DC current information of the pixels allows a precise determination of the mispointing at a given hour angle and declination. This procedure can be repeated for many hour angles and declinations. A correction based on values obtained from this procedure improved the Mispointing but did not yield completely satisfactory results and a ***different strategy*** has been tried here in this thesis.

The false source plot method

A mispointing correction can also be obtained by ***only*** using the measured data of ***Mkn 421.*** The construction of a false source plot is a simple method to find the ***real position*** of a source in the camera. Since the coordinates for Mkn 421 are known the ***mispointing*** can be calculated.

The algorithm proceeds as follows: The camera center is ***moved*** artificially (and ALPHA is recalculated accordingly) in a grid around the camera center. A ***cut*** of $ALPHA_{new}$ <8° is applied to the new ALPHA value for each position and the remaining events are ***filled*** in a 2D histogram which binned ***according*** to the grid. After the histogram has been filled, a tail-cut at the half maximum is performed by subtracting the half maximum from each bin. Bins below zero are set to zero. The position of the source is obtained by calculating the ***mean*** of the 2D histogram.

The new ALPHA is calculated from the old (signed) ALPHA as follows (see Fig. A.36):

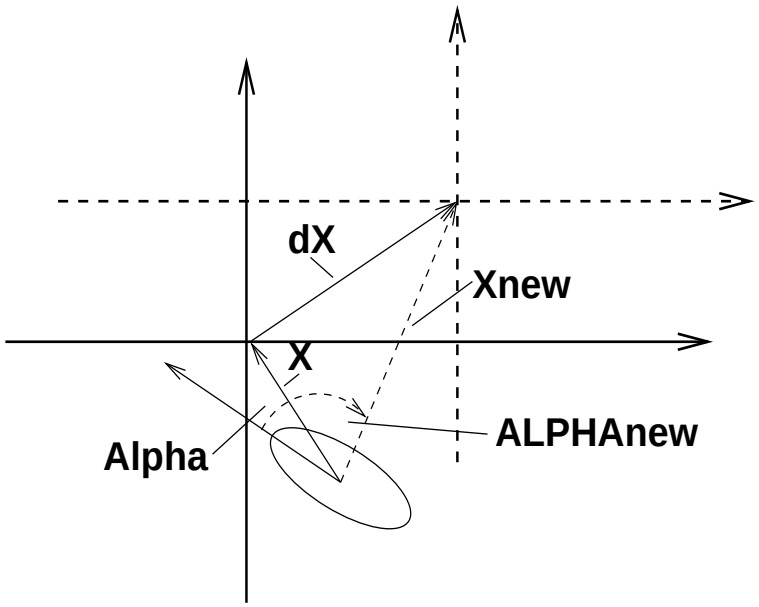

Figure A.36: Schematic of the shift of the old coordinate system and the calculation of the new ALPHA.

$$\overrightarrow{Alpha_{old}} = \begin{pmatrix} \cos\alpha_{old} & -\sin\alpha_{old} \\ \sin\alpha_{old} & \cos\alpha_{old} \end{pmatrix} \overrightarrow{\langle X_{old}\rangle} \quad \text{(A.92)}$$

$$\overrightarrow{\langle X_{new}\rangle} = \overrightarrow{\langle X_{old}\rangle} + \overrightarrow{dX} \quad \text{(A.93)}$$

$$ALPHA_{new} = \arccos \frac{\overrightarrow{Alpha_{old}} \cdot \overrightarrow{\langle X_{new}\rangle}}{\left|\overrightarrow{Alpha_{old}}\right| \cdot \left|\overrightarrow{\langle X_{new}\rangle}\right|} \quad \text{(A.94)}$$

First a vector pointing in the direction of the shower $\overrightarrow{Alpha_{old}}$ is obtained by rotating the mean position vector $\overrightarrow{\langle X_{old}\rangle}$ of the image by ALPHA ($ALPHA_{old}$). The new position vector $\overrightarrow{\langle X_{new}\rangle}$ is calculated by translating the old center with $\overrightarrow{dX}$. The new ALPHA $ALPHA_{new}$ (unsigned) is obtained from the scalar product of the old direction vector and the new position vector.

Binning the data in (signed) zenith angles

The mispointing is assumed to be a function of the hour angle and the inclination. The inclination remains ***constant*** for astronomical objects. Since the parameter hour angle was not available in the dataset a binning in ***signed*** zenith angle was performed instead (positive sign for azimuth angles larger than 180°, and negative sign for azimuth angles smaller then 180°). This binning is ***equivalent*** to binning in shaft-encoder values (and to the hour angle) of the telescope.

For ***each*** signed zenith angle bin a ***false source plot*** is calculated. By examining the false source plots one can see that for high zenith angles especially the pointing is ***not sharp*** in one spot (see Fig. A.35). This effect could be partly due to ***statistics***, but as we will see a mispointing correction on run basis results in a sharper ALPHA distribution, suggesting that for different runs with identical hour angle (equivalent to 'signed' zenith angle) the mispointing is different.

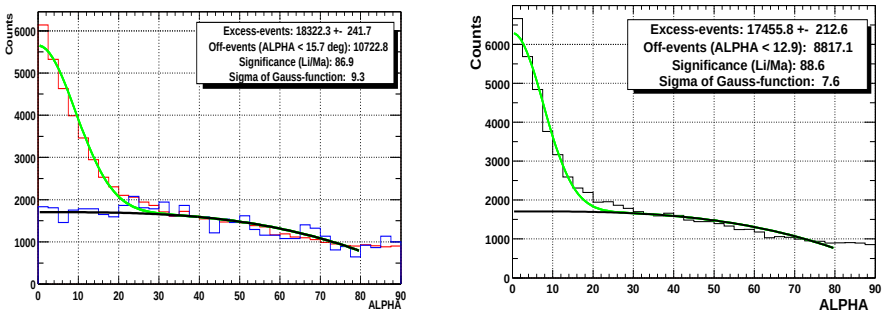

Figure A.37: a) The ALPHA distribution before applying the pointing correction. The sigma of the ALPHA peak is 9.3°. The Off-data distribution (much lower statistics) has been included into the plot for illustration. b) The ALPHA distribution after applying the pointing correction procedure. The distribution gets significantly sharper. The average sigma of the (full) Gaussian fit curve is only 7.6° . The tail of the ALPHA distribution between 20° and 30° does not fit very well to the Gaussian function. This is caused by a still imperfect mispointing correction. The high zenith angles have a wider ALPHA distribution. To avoid confusion it has to be stated that he data used here is the full dataset of Mkn 421 of 250 hours of observation time. This dataset contains more signal than the test data set used for the development of an improved analysis.

Binning in runs

To circumvent this problem, in addition a pointing correction for each run was introduced. A false source plot was then calculated for ***each run***. The correction in run bins is ***only possible*** if there is ***enough*** signal in that specific run data (the problem of a flaring source). The procedure applied was the following: If the signal in the run data was ***too small*** (smaller than ***5 sigma*** of the background fluctuations), the pointing correction on ***zenith angle bin*** basis was applied (the zenith angle bins have a ***much larger statistics and*** there is ***no danger*** of optimizing on fluctuations). If the signal was large enough during that run (larger than ***5 sigma***) then the mispointing ***based on single run*** bins is chosen. The mispointing correction on a ***run to run basis*** improves the sharpness of the ALPHA distribution significantly when compared to a mispointing correction on the basis of ***signed zenith angles*** only. This seems to point out that the mispointing for the same hour angle but on different days is different.

Results of the mispointing correction

Tab. A.7 shows the results ***after*** the pointing correction. Listed are the ***variances*** of the alpha distribution for each signed zenith angle bin. The total standard deviation was improved from ***9.3***° (before correction) to ***7.6***° (after correction). The correction on the basis of signed zenith angle bins only gave a standard deviation of approximately ***8.3***°. The table clearly shows how the alpha distribution becomes wider with ***increasing*** zenith angle. For ***all*** zenith angle bins the alpha distribution is ***wider*** than the corresponding distribution in the ***MC*** which points to still ***imperfect*** mispointing correction.

Conclusion

In conclusion, it can be stated that the result is still ***not perfect***. The variances of the alpha peak should be ***more narrow***. However, they are ***good enough*** to ensure a reasonable (without systematics coming from the ALPHA distribution) lightcurve. In the following chapters all of the cuts on the alpha distribution are performed very high at 18°. In this

Signed zenith angle	Sigma of alpha distribution
-(45-50)	10.3 ± 0.15
-(35-45)	8.9 ± 0.10
-(25-35)	6.7 ± 0.12
-(15-25)	7.0 ± 0.11
(-15)-(+15)	7.2 ± 0.13
15-25	7.4 ± 0.07
25-35	8.1 ± 0.11
35-45	8.6 ± 0.15
45-50	8.9 ± 0.18
Total	7.6 ± 0.08

Table A.7: The table shows the final variances of the ALPHA distribution for different zenith angle bins. The variances increase with increasing zenith angle.

way it can be made sure that most of the signal events are inside the cut limit and that the resulting measured flux no longer depends on the zenith angle.

The spectrum before and after applying this pointing correction remains the same which can be taken as a proof that no artificial effect has been introduced by optimizing on fluctuations.

A.7 Differential flux spectrum calculation

The differential flux is one of the main physical quantities that we are interested in. It is a measurement which can be compared with the theory and that tells us something about the mechanism that produces jets and high energy gammas inside the jet. The calculation of the differential flux is a rather complicated procedure that involves several steps.

1. The energy of the observed events is reconstructed. Then the ***excess events*** N^i_{Excess} for different energy bins are determined by estimating the background in each energy bin (this results in the ***excess event distribution***). The reconstructed energy can derivate, both systematically and statistically, from the true one.

2. Therefore the spectrum calculation requires the ***unfolding*** of these effects (of the excess event distribution).

3. Finally, the ***differential flux*** is obtained by dividing each bin by the total observation time T_{obs}, the bin width ΔE_{Bin} and its effective collection area. The observation time has to be taken separately for each zenith angle bin.

$$\frac{dF^i}{dE} = \frac{\Delta N^i_{Excess,unfolded}}{\Delta E^i_{Bin} \sum_{\theta_i} T^{\theta_i}_{obs} A^i_{eff}(\theta_i)} \tag{A.95}$$

A.7.1 Determination of the energy excess event distribution

The energy excess event distribution is the ***first step*** to the differential flux spectrum (dF/dE). The events are sorted in energy bins according to their estimated energy. The binning has been chosen to be of the size of the average energy resolution (~24 %). In ***logarithmic scale a constant binning*** (for simplicity) was introduced. The resolution is to first order constant in this frame (See Fig. A.38).

For each energy bin, a histogram for the ***ALPHA*** distribution was filled and the corresponding background was estimated by performing ***a fit*** as was done earlier.

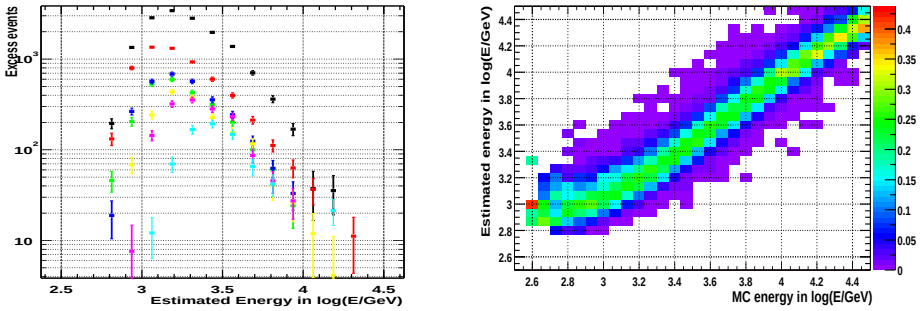

Figure A.38: a) This figure shows the ***excess event distribution*** of the total ***Mkn 421*** data set for all ***six*** zenith angle bins in different colors (red: 0°-16°, blue: 16°-21°, green: 21°-28°, yellow: 28°-33°, violet: 33°-40°, light blue: 40°-50°, black: all together). The figure illustrates how the threshold ***changes*** with zenith angle. Due to ***different*** observation times the total amount of excess events is different for different zenith angles. The black points are the ***sum*** of the data of all the zenith angles. b) The estimated energy and the MC energy are plotted against each other and normalized to one (Probability distribution of the estimated energy). It demonstrates that in first order the resolution ***is constant in logarithmic scale***. The curved shape of the distribution for energies below 1 TeV is corrected later on by the unfolding procedure.

$$N^i_{Excess,Data} = N^i_{Alpha<15\,deg} - N^i_{Backgound<15\,deg} \tag{A.96}$$

The ALPHA distributions and their background fit are listed in Appendix B. The systematic error introduced by the background estimation is believed to be smaller than 5%-10%. The effect of all possible systematic errors, which can affect the spectrum, will be discussed in detail in the conclusion. As will be shown, the spectral shape remains ***virtually unchanged*** by artificial changes in the amount of background of +-10%.

The energy distribution of the excess events can be seen in Fig. A.38. The different zenith angles are represented by different colors (red: 0°-16°, blue: 16°-21°, green: 21°-28°, yellow: 28°-33°, violet: 33°-40°, light blue: 40°-50°, black: all together). As expected the threshold increases with increasing zenith angle.

A.7.2 Unfolding the spectrum

The spectrum of a real source should be ***unfolded*** with the distribution of the estimated energy. This is important not only to correct for ***nonlinearities in the energy estimation***. It also corrects for ***spill over*** from each energy bin into the neighbor bins on the left and right side and a possible cutoff would change its position.

The energy estimation allows us to determine the transfer function of the telescope as the simulation describes the total system. As in Fig. A.34, we can fill a matrix $\mathbf{M}$ which yields us for each (real, simulated) energy bin the ***probability distribution*** (normalized to one) of the estimated energy. Naturally, the binning of $\mathbf{M}$ and the binning of the excess event distribution (i.e. data distribution D_k) must be the same. Knowing $\mathbf{M}$ we can can calculate the spectrum of the ***folded*** spectrum $\vec{F}$ for a given ***unfolded*** spectrum $\vec{U}$:

$$\mathbf{M}\vec{U} = \vec{F} \tag{A.97}$$

The reverse of this procedure is called ***unfolding:***

$$\mathbf{M}^{-1}\vec{F} = \vec{U} \tag{A.98}$$

Even though this procedure is mathematically valid, it does not usually yield decent results. Since the spectrum vector $\overrightarrow{F}$ and M also has statistical fluctuations (it has been determined by Monte Carlo studies), the resulting vector tends to artificial ***oscillations*** between ***neighboring vector entries*** (in 'energy'-space). There are various methods available which attempt to suppress these completely unphysical high frequencies by means of regulators or low pass filters in the frequency space.

The method used here is a stepwise ***iterative method*** which is especially suitable for our situation. It is described in [Des95]. The procedure has been slightly modified to work efficiently for our case. The algorithm systematically ***adjusts*** the ***folded MC*** distribution F_k to the ***real data*** distribution D_k until the chisquare between the two distributions becomes ***minimal.*** The original ***unfolded MC*** distribution is then the distribution that we are interested in. The regulation here consists of ***interrupting*** the iteration before it can develop high frequency oscillations.

The exact procedure is as follows:

1. First a ***initial*** unfolded spectrum is ***estimated***. The closer the initial distribution to the final result, the better the convergence. In this case simply the ***folded data spectrum*** is taken (along with its errors) since it is already very similar to the expected unfolded result.

2. In an ***iterative loop*** the following steps l are executed for each bin i:

   (a) The ***folded spectrum*** is calculated from the unfolded distribution with (same as above)
   $$F_k^l = \sum_i \mathbf{M}_{ik} U_i^l \tag{A.99}$$

   (b) The ***ratio*** of the folded MC F_k and the real data distribution D_k is ***back-propagated*** into proportional factors λ_i
   $$\lambda_i^{l+1} = \sum_k \mathbf{M}_{ik} \left(\frac{F_k^l}{D_k^l} \right)^{\alpha_k} \tag{A.100}$$
   which are then applied to the ***unfolded data*** distribution
   $$U_i^{l+1} = N^{l+1} \lambda_i^{l+1} U_i^l \tag{A.101}$$
   in such a way that the ***folded*** MC distribution ***converges*** to the ***real*** data distribution. The row vectors (estimated energy distribution) of the matrix M_{ik} must be normalized in a manner such that for each index i the sum over all entries k give one. N^{l+1} is a normalization factor which ensures that the integral over the previous spectrum and after application of the proportional factors λ_i is preserved.

   (c) The ratio Equ. A.100 is potentiate with ***exponents*** $\alpha_k \in [0,1]$ which depend ***monotonically*** on the difference between the data distribution and the folded MC distribution, weighted by its error (χ^2 for one bin), in order to achieve ***smooth*** and equivalent ***convergence simultaneously*** along the ***entire*** spectrum.
   $$s_k = \frac{\left(F_k^l - D_k^l\right)^2}{\sigma^2_{F_k^l} + \sigma^2_{D_k^l}} \tag{A.102}$$
   $$\alpha_k = Sigmoid\,(s_k) \tag{A.103}$$
   $$Sigmoid\,(x) = \left(\frac{2}{1+e^{-x}} - 1 \right) \in [0,1] \tag{A.104}$$

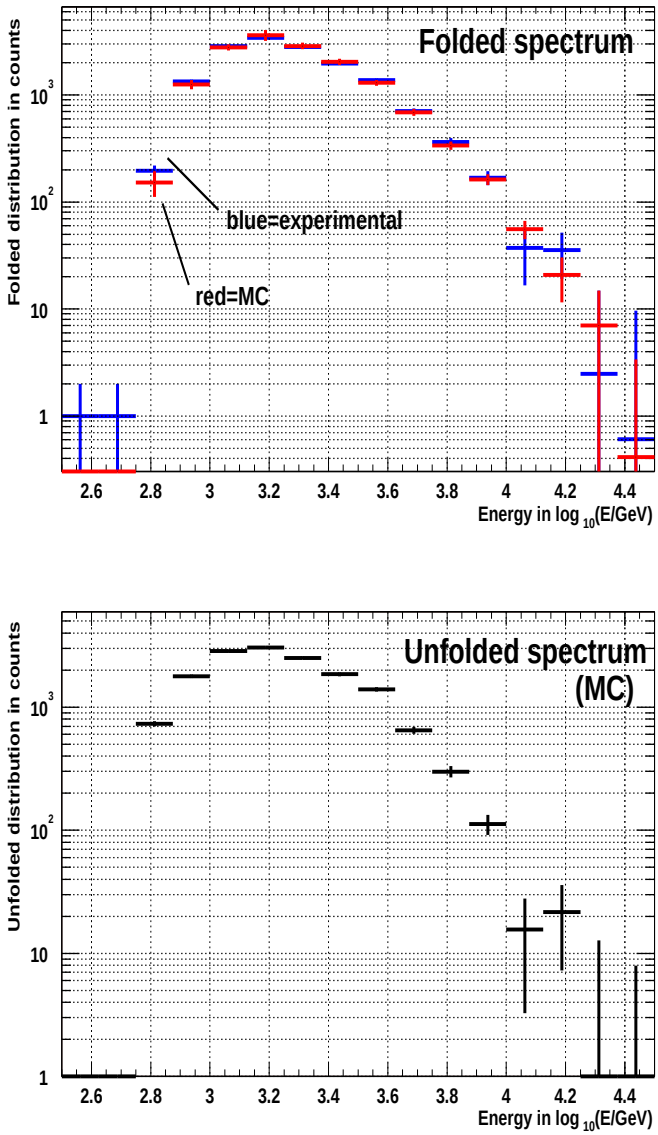

(a) Unfolded spectrum

Figure A.39: The unfolding procedure is illustrated in the two plots. a) The experimental distribution (blue) is stepwise approximated by a folded MC distribution (red). b) The unfolded MC distribution is shown in the plot below. a) The folded spectrum changes its shape after unfolding especially in the energy region below 1 TeV and above 10 TeV ($log(E/GeV) = 4.0$) the cutoff appears stronger. Above $log(E/GeV) = 4.2$ the method becomes inaccurate due to very low statistics.

The sigmoid-like function has been introduced to assure that the exponents α_k are within the interval $[0, 1]$. Excessively large α_k values accelerate the convergence up to a point where the oscillations can no longer be controlled.

(d) The errors on the unfolded spectrum are calculated by ***Gaussian error propagation*** from the involved unfolded data bins and from the error on the transfer matrix M_{ik}.

(e) The χ^2 of the difference between the data spectrum D and the folded MC F is computed for each step

$$\chi^2 = \sum_k s_k \tag{A.105}$$

in each step. When the χ^2 starts to ***increase*** the iteration procedure terminates.

3. The procedure converges rapidly within ***five*** iterations. However, after a maximum of ***eight*** iterations the procedure is terminated to ensure that the high frequency oscillations do not develop.

Conclusion

The procedure begins with the excess event distribution obtained by using the energy estimation described above. The iteration process corrects the spectrum for ***nonlinearities*** and biases that were introduced by the energy estimation. In particular, it corrects for ***spill over*** effects from lower energy bins into higher energy bins. Without application of this unfolding procedure, the resulting spectrum would be flatter than the true one and a possible cutoff would be measured at a wrong position.

Because of statistical effects the unfolding procedure can ***only approximate*** the true spectral shape. This has been ensured by using the exponents α_k which are obtained by weighting with the variances (i.e. statistical fluctuations) in each bin.

The resulting distribution fits better to the effective areas that were obtained by MC studies as experience showed. Fig. A.39 demonstrates the result. The upper plot shows the original data distribution and the folded MC distribution. The lower plot shows the unfolded spectrum. Above 20 TeV virtually no significant signal (too low statistics) is seen so that this part of the distribution is discarded.

A.7.3 The spectrum, fitting and reverse check of the result

The data has been sorted into ***several zenith angle bins*** because the effective collection areas and the telescope threshold vary with zenith angle. The ***observation times*** for each zenith angle bin were carefully determined. In addition to the spectra for each zenith angle, ***the total spectrum*** was calculated by computing the effective areas and the normalized inversion matrix $\mathbf{M}_{ik}$ for the given zenith angle distribution as found in the dataset.

Fig. A.40 shows in the upper plot the spectrum of the crab nebula and in lower plot its excess event distribution which was used to obtain the spectrum. The spectrum (upper plot) has been fitted with a normal power law ansatz:

$$\frac{dF_{PowerLaw}}{dE} = F_0 E^{-\alpha} \tag{A.106}$$

with a differential spectral index α and a flux constant F_0. The ***fit results*** here are $F_0 = (3.0 \pm 0.3)10^{-11} TeV^{-1} cm^{-2} s^{-1}$, $\alpha = 2.5 \pm 0.1$ with a χ^2/NDF=5.5/9.

Since unfolding processes in general are ***not completely satisfactory*** and mathematically stable one might wish to ***cross check*** the obtained results. Therefore also the reverse process was also examined. Out of a given differential flux the expected number of excess events per energy bin $\left[E^k_{left}, E^k_{right}\right]$ can be computed:

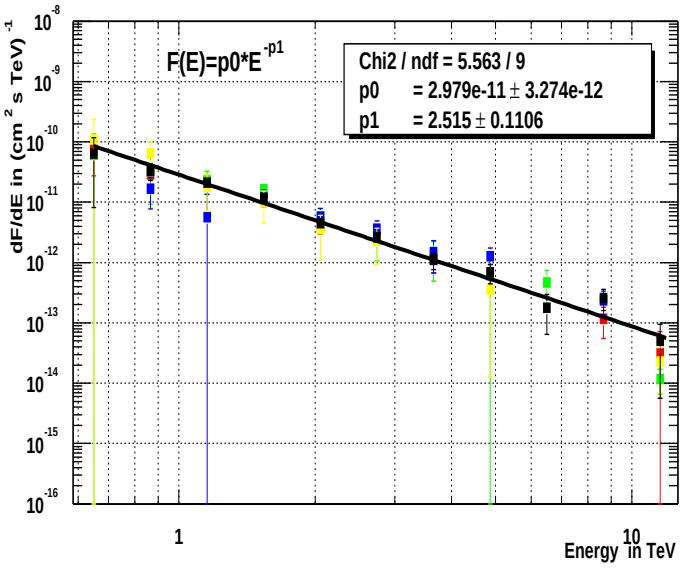

(a) Crab spectrum

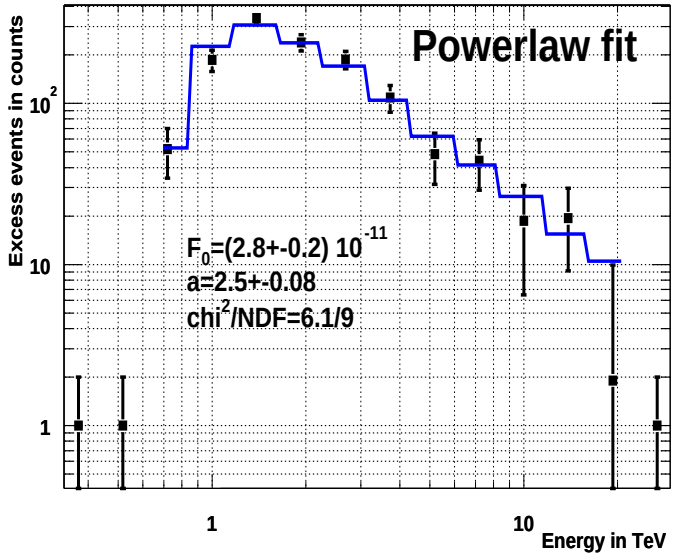

(b) Excess event distribution

Figure A.40: a) The upper plot shows the unfolded spectrum of the Crab nebula. The fit results here are $F_0 = (3.0 \pm 0.3)\, 10^{-11} TeV^{-1} cm^{-2} s^{-1}$, $\alpha = 2.5 \pm 0.1$ with a χ^2/NDF=5.5/9.
b) The plot shows the experimental excess event distribution of the Crab nebula. The theoretically expected excess event distribution for a power law spectrum (blue curve) has been fitted to the original excess event distribution (data points). Mathematically, this is more satisfactory because, as opposed to an unfolding process, is involved a folding process in this case and the expected errors are smaller. The fit results are: $F_0 = (2.8 \pm 0.2)\, 10^{-11} TeV^{-1} cm^{-2} s^{-1}$, $\alpha = 2.5 \pm 0.08$ with a χ^2/NDF=6.1/9. The values are consistent with the result from the upper plot. The fit error are slightly smaller due to the unfolding procedure applied in the upper plot. The Crab nebula is usually used as a standard candle and as a cross check to compare analysis results with other γ-ray experiments.

$$N^{Expec}_{Excess,i}\left(F0, \alpha\, E_{cut}, \beta\right) = \tag{A.107}$$
$$T_{obs} A_{eff,i} \sum_k \mathbf{M}_{ik} \int_{E^k_{left}}^{E^k_{right}} \frac{dF\left(F0, \alpha\, E_{cut}, \beta\right)}{dE} dE$$

The reverse process does not need an ***unfolding*** algorithm of the data spectrum, but rather a ***folding*** algorithm of an assumed unfolded spectrum. Mathematically, this is much more satisfactory, reliable and precise. A folded power law function has been fitted to the original excess event spectrum and can be seen in Fig. A.40 (lower plot). The ***fit results*** are: $F_0 = (2.8 \pm 0.2) 10^{-11} TeV^{-1} cm^{-2} s^{-1}$, $\alpha = 2.5 \pm 0.08$ with a χ^2/NDF=6.1/9. Both methods give practically the same fitting results and are therefore ***consistent.*** The fit to the original folded excess event distribution gives more precise results and ***smaller fitting errors.***

A.7.4 Discussion of systematic errors and the reliability of the obtained spectrum

The results of the analysis depend on several potential systematic errors which are discussed here.

1. The ***first*** error comes from the ***calibration of the absolute energy scale***. The pixels in the camera were calibrated by the so-called ***excess noise factor method*** which was already described above. Due to several unknown parameters and uncertainties, a miss-calibration of the absolute energy scale of up to 15 % is easily possible.
   A forced translation of the energy scale by a small amount (+- 10 %) changes the position of the threshold of the telescope relative to the threshold in the effective areas which consequently changes the shape of the spectrum in the region of the left slope of the excess event distribution. The resulting spectrum is no longer linear and results in a curved spectrum (in the threshold region), in either an upward or downward direction.
   However the total shape of the calculated spectrum is ***not very sensitive to a change of 10 %.*** The spectral index of the differential flux changes slightly. The spectrum of the crab nebula shows a clear ***power law*** spectrum as it should without any distortion of the power law close to the threshold. For this reason it is believed that the calibration of the absolute energy scale is ***not worse*** than 10 %.
   The change in the slope by artificially changing the energy scale by +-10% is only about $\sigma_{sys}(\alpha) = \pm 0.1$ for a spectral index of approximately $\alpha = 2.5$. Due to the uncertainty in absolute energy scale a possible cutoff position (Mkn 421) cannot be determined ***more precisely*** than approximately $\sigma_{sys}(E_{cut}) = \pm 1\, TeV$.

2. The ***second*** systematic error originates in the ***estimation*** algorithm for the ***background.*** The estimated miss-determination of the background is believed to be ***less*** than 10%. Surprisingly, a forced change of $\pm 10\%$ in the estimated background did not produce any ***significant change*** in the steepness of the spectrum. But for a forced overestimated/underestimated background the ***cutoff position*** (for Mkn 421) moves down/up by approximately $\sigma_{sys}(E_{cut}) = \pm 1\, TeV$. However, comparisons with the flux of the HEGRA CT-System and correlation studies with the RXTE/ASM satellite show that the origin of this analysis coincides with the ***origins*** of the other instruments. Therefore it is believed that that the background estimation is ***better*** or equal than 5%.

3. The ***third*** systematic error originates from the calculation of the effective areas which are calculated by applying the same ***selection cut*** to the data and to the MC.

This assumes that the MC describes showers and their imaging in a reasonable way. Systematic errors on the absolute flux due to slightly wrong effective areas are estimated to be approximately ***10 %*** or $\sigma_{sys}(F_0) = \pm 0.1\, F_0$.

A.8 Calculation of lightcurve and hardness ratio

The lightcurve is another important measurement which provides us with valuable information about the time structure of the flares of Mkn 421. It gives us hints about the size of this object and its emission regions and about the mechanisms that produce high energy gammas (SSC).

A.8.1 The mathematical background of integrated flux measurements

The ***lightcurve*** (Fig. A.41) consists of integrated flux measurements for small time bins:

$$F_{[E_{min},E_{max}]}(t) = \frac{dN}{dA\,dt} = \int_{E_{min}}^{E_{max}} \frac{dF(t)}{dE} dE \tag{A.108}$$

The so-called ***hardness ratio*** is the ratio of integrated fluxes of two energy intervals, an upper energy interval and a lower energy interval

$$R(t) = \frac{F_{\left[E_{min}^{upper},E_{max}^{upper}\right]}(t)}{F_{\left[E_{min}^{lower},E_{max}^{lower}\right]}(t)} \tag{A.109}$$

It is used to detect changes in the steepness of the spectrum, which might change with flare intensity.

For the lightcurve, the data is binned with the ***granularity a single run***. For each run bin, the duration T_{obs}, the average zenith angle θ and the center noon-MJD t are found. ***Three*** different ***energy intervals*** were treated simultaneously.

1. For the ***normal lightcurve***, an interval $[1.0, 20]$ TeV was taken. A hard cut at $E_{est} > 1.0$ TeV was applied in order to leave out the region that is too close to the energy threshold of the telescope so that the systematic error in the lightcurve could be reduced. This region is very sensitive to the zenith angle because of strongly varying collection areas there.

2. The other ***two energy intervals*** are needed for the ***hardness ratio*** calculation and are kept variable (this will be discussed later).

The ***excess-rate*** $Rate_{Excess}(t)$ and the background-rate $Rate_{Off}(t)$ are

$$Rate_{Excess}(t) = \frac{N_{On}(t) - N_{Off}(t)}{T_{obs}} \tag{A.110}$$

$$Rate_{Off}(t) = \frac{N_{Off}(t)}{T_{obs}} \tag{A.111}$$

The ***'On'-events*** are the events for which ALPHA is ***smaller than 18***°. The cut on ALPHA was chosen to be ***very generous*** in order to ensure that most signal events were retained so as to ***reduce*** the systematic error on zenith angle dependence (as was already mentioned above). The background events between 0° and 18° are ***estimated*** by fitting the ALPHA distribution for each run between 20° and 80° ***only*** with a polynomial. Due to low statistics, the ALPHA peak was not fitted with a Gaussian in this case.

The background rate is ***useful*** to detect ***corrupted*** runs (from bad whether or other problems). The background rate is slightly dependent on the zenith angle and decreases

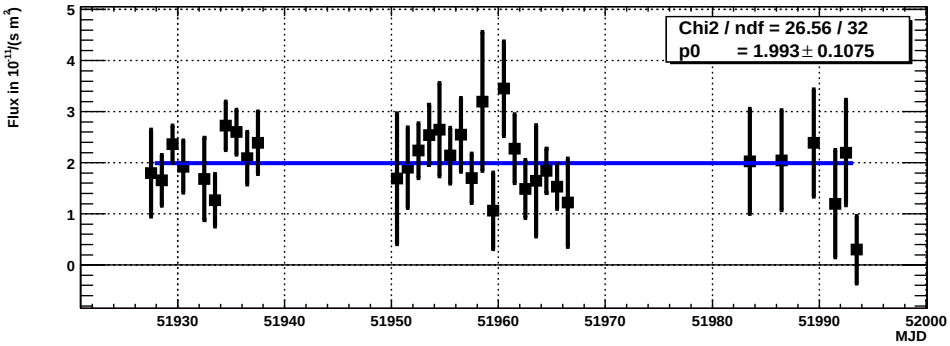

(a)

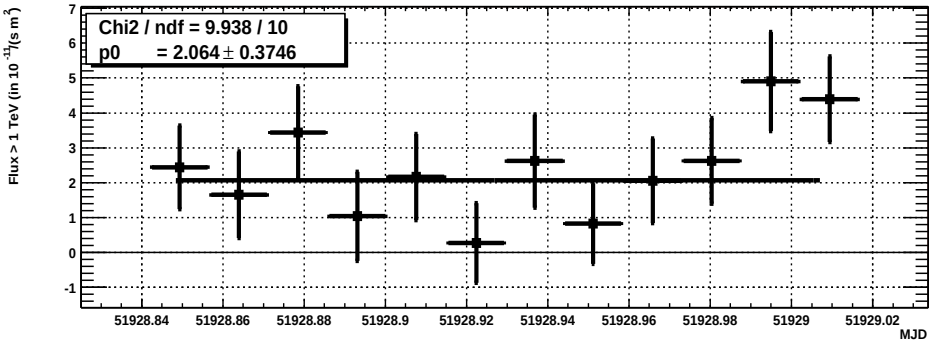

(b)

Figure A.41: a) The light curve of the crab nebula from February to April 2001 averaged over one day bins and b) an example light curve of the crab nebula of one night with run flux points. The crab nebula emits a constant flux. According to the χ^2 value, the fluctuations are in the order of magnitude which would be expected from the errors on the flux points. This tells us that the error calculation of the lightcurve is consistent with the observed fluctuations.

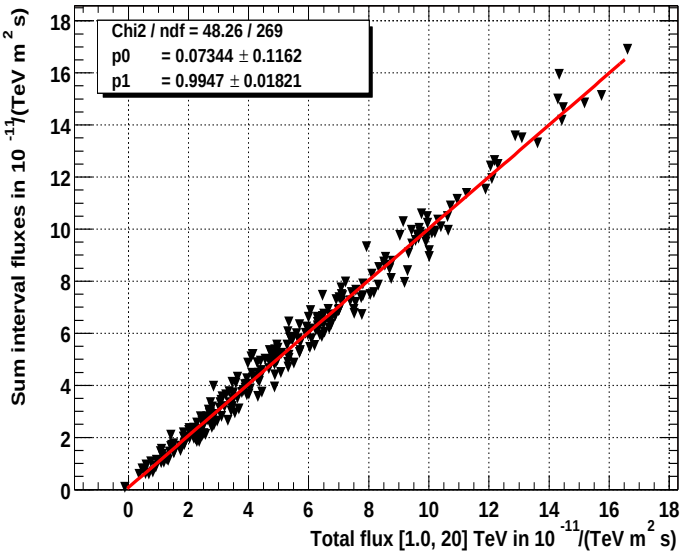

Figure A.42: ***Consistency check*** of ***lower energy*** interval flux ([1.0, 2.0] TeV) and ***higher energy*** interval flux ([2.0, 20] TeV) calculation (for the Mkn 421 data set). The ***sum of both*** fluxes is plotted against the ***total flux*** (energy interval [1.0, 20.0] TeV). The background estimation and also the effective area calculation for the curved spectrum is done separately for the different energy intervals. The plot proves ***consistency*** of the sum and the total.

with increasing zenith angle. All the runs with background rates of ***less than 10 events/hour*** (usually the rates are in the order of 40 events/hour) are ***rejected*** in a quality selection cut.

Hence, the ***integrated flux*** for a given energy interval is defined as the excess rate for this energy interval divided by its ***average effective area*** for the corresponding zenith angle:

$$F_{[E_{min},E_{max}]}(t) = \frac{Rate_{Excess,[Emin,Emax]}\,(t)}{A_{eff,int}\,(\theta)} \tag{A.112}$$

In order to obtain the average effective area the ***differential fluxes*** from the spectrum calculations are used because these numbers are ***very dependent*** on the ***shape*** of the spectrum. The effective area is ***interpolated*** for the zenith angle needed. The average zenith angle changes from run to run. Figure A.42 shows in a cross check the consistency of the flux calculation. The sum of the lower energy [1.0, 2.0] TeV and higher energy [2.0, 20] TeV interval fluxes are plotted against the total flux (energy interval from [1.0, 20] TeV).

The average effective area is a ***weighted average*** of the flux summed over all energy bins inside the given interval [WitCom].

$$A_{eff,int}\,(\theta) = \frac{\sum_{E^i\in[E_{min},E_{max}]} \frac{dF}{dE}\left(E^i\right)\cdot(E_{max}-E_{min})\cdot A_{eff}\left(E^i,\theta\right)}{\sum_{E^i\in[E_{min},E_{max}]} F^i}$$

The events are sorted into the ***energy intervals*** by using the estimated energy. For this calculation of the lightcurve ***no unfolding*** was performed due to ***very low statistics***. Since rather large energy intervals are integrated, this should not introduce excessively large systematic errors. The only potential systematic error originate from the region of the energy threshold that is ***largely excluded*** (with the cut at 1 TeV).

The error in the flux is derived from Gaussian error propagation and its nature is purely statistical.

$$\sigma^2_{Rate} = \frac{N_{On} + N_{Off}}{T^2_{obs}} \quad \text{(A.113)}$$

$$\sigma^2_F = \frac{\sigma^2_{Rate} + F^2\sigma^2_{Aeff}}{A^2_{eff,int}} \quad \text{(A.114)}$$

A.8.2 Discussion about systematic errors and the reliability of the measured lightcurve

Two potential systematic errors can influence the lightcurve measurement.

1. The first one results from the ***impossibility*** of performing an unfolding procedure on the basis of run, due to a lack of available statistical information. This error can be significantly ***reduced*** a lot by performing a hard cut on the lower energy region.

2. The second one is related to the ***background estimation***. As explained in the section concerning the differential flux measurement, a maximum systematic error of 10% is assumed. However, comparing the flux results to the one of the HEGRA CT-system and also to correlation studies with the RXTE/ASM satellite (both in the next chapter) show that the ***origin*** of the flux calculation is in good agreement with the other two instruments. For this reason it is believed that the background estimation is better than or equal to 5%.